50th AIAA Aerospace Sciences Meeting including the New Horizons Forum and Aerospace Exposition
09 - 12 January 2012, Nashville, Tennessee

AIAA 2012-1013

Aerodynamic Interactions of Reaction Control System Jets on Mars Entry Aeroshells

Hicham Alkandry[*] and Iain D. Boyd[†]

Department of Aerospace Engineering, University of Michigan, Ann Arbor, MI, 48109

Erin M. Reed[‡], Joshua R. Codoni[§], and James C. McDaniel[¶]

Department of Mechanical and Aerospace Engineering, University of Virginia, Charlottesville, VA, 22903

The fluid interactions produced by a sonic reaction control system (RCS) thruster for a Mars-entry aeroshell are investigated using computational fluid dynamics (CFD). The study uses a scaled Mars Science Laboratory (MSL) aeroshell at a 20° angle-of-attack in Mach 12 flow of I_2-seeded N_2 gas. The RCS jet is directed either parallel or transverse to the freestream flow in order to examine the effects of the thruster orientation with respect to the center of gravity of the aeroshell. The results show that both the parallel and transverse RCS jets obstruct the flow around the aeroshell and impinge on the surface, which increase the overall pressure on the aftbody. As a result, the RCS jet decreases both the drag and lift forces, and the moment acting on the aeroshell, particularly at relatively large RCS thrust conditions. The results also indicate that the fluid interactions produced by the parallel and transverse jets affect the control effectiveness of the RCS. The performance of the parallel RCS thruster is close to ideal due to relatively small aerodynamic interference induced by the jet. However, the relatively large aerodynamic interference produced by the transverse RCS jet causes a deficit of control authority. The physical accuracy of the computational method is assessed by comparing the numerical results with experimental visualizations.

Nomenclature

symbols

C_A	Axial Force Coefficient	M_z	Moment [N·m]
C_D	Drag Coefficient	$\dot{m}$	Mass Flow Rate [kg/s]
C_f	Skin Friction Coefficient	P	Pressure [Pa]
C_L	Lift Coefficient	q	Dynamic Pressure [Pa]
C_M	Moment Coefficient	Re	Reynolds Number
C_N	Normal Force Coefficient	S	Aeroshell Frontal Area [m²]
C_P	Pressure Coefficient	U	Velocity [m/s]
C_T	Thrust Coefficient	X	Mole Fraction
Kn	Knudsen Number	ρ	Density [kg/m³]
L/D	Lift-to-Drag Force Ratio	τ	Shear Stress [Pa]
M	Mach Number		

subscripts

0	Total (Stagnation) Conditions	ref	Reference Freestream Conditions
jet	RCS Jet Conditions		

---

[*]Graduate Student, Student Member AIAA.

[†]James E. Knott Professor, Fellow AIAA.

[‡]Graduate Student, Student Member AIAA.

[§]Graduate Student, Student Member AIAA.

[¶]Professor, Associate Fellow AIAA.

American Institute of Aeronautics and Astronautics

I.   Introduction

THE Mars Science Laboratory (MSL) will make the first attempt at performing precision landing on Mars.[1] The guided lifting entry of MSL will use a reaction control system (RCS), shown schematically in Figure 1, for both rate damping and guidance maneuvers as required throughout most of the entry, including the hypersonic regime.[2] As a result, the landing accuracy for MSL will increase from within hundreds of kilometers for past Mars missions (e.g. Viking and Pathfinder) to within tens of kilometers. Precision landing on Mars using RCS jets will also be crucial for future human exploration missions, which will require landing accuracy to within tens of meters from their targets[3] to either land near pre-deployed cargo, or land at scientifically interesting sites that may be surrounded by surface hazards, such as rocks and craters. The use of RCS thrusters, however, generates complex fluid interactions between the jets, the wake, and the aeroshell which can affect the flowfield, surface, and aerodynamic properties of the entry capsule.
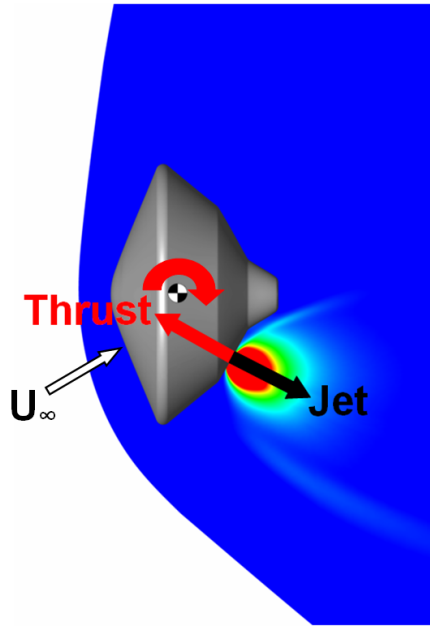

Figure 1.   Illustration of a Mars-entry aeroshell with a reaction control system.

A significant amount of work has been performed to analyze the fluid interactions induced by the reaction control system for MSL.[2,4–7] These studies have had a significant impact on the design of the MSL RCS thruster layout, which evolved due to several constraints including aerodynamic interference.[2] Even with this work, however, there is still a need for more validated numerical methods and further experimental tests in order to mature the reaction control system as a reliable technology for future Mars missions.[2] Therefore, the goal of this study is to continue the development of RCS by investigating the fluid interactions induced by a sonic RCS thruster in hypersonic freestream conditions using computational fluid dynamics (CFD). In this study, the RCS jet is directed either parallel or transverse to the freestream flow in order to examine the effects of the thruster orientation with respect to the center of gravity of the aeroshell. The physical accuracy of the computational method is assessed by comparing the numerical results with experimental data.[8] The paper first describes the numerical and experimental techniques, as well as the conditions used in this study to examine the interactions produced by the RCS jet. The paper then presents the numerical results for the baseline configuration without the RCS jet. Next, the paper describes the effects of the RCS jets on the flowfield, surface, and aerodynamic properties of a Mars-entry capsule, as well as the effects of these interactions on the control effectiveness of the reaction control system. Finally, the paper presents qualitative comparisons between the numerical results and experimental visualizations.

American Institute of Aeronautics and Astronautics

II.   Technical Approach

A.   Experimental Technique

The conditions simulated in this study are based on experimental conditions obtained from on-going work conducted at the University of Virginia[8] in order to compare the numerical results with the experimental data.   The hypersonic flow facility at the University of Virginia is capable of providing Mach numbers and Knudsen numbers up to 16 and 1, respectively. Hypersonic flow from an under-expanded jet, shown schematically in Figure 2(a),[9] is produced by the expansion of iodine-seeded nitrogen gas through a thin circular orifice of diameter $D = 2$ mm into a continuously evacuated vacuum chamber. The freestream Mach number and flow properties can be changed by adjusting the distance of the test model to the orifice. Figure 2(b) shows calculated variations of Mach number and Knudsen number (Kn) based on the orifice diameter in the experimental test section.[10] These contours show the barrel shock that develops at the entrance of the test section and terminates at the Mach disk. Models are placed in the under-expanded jet core for testing at hypersonic conditions. The stagnation pressure and temperature in the wind tunnel are 1.8 atm and 297 K, respectively. Although this facility is capable of providing Mach numbers and Knudsen numbers that are similar to those encountered during atmospheric entry, it does not generate enthalpy levels as high as those achieved during flights due to the relatively low stagnation temperature.
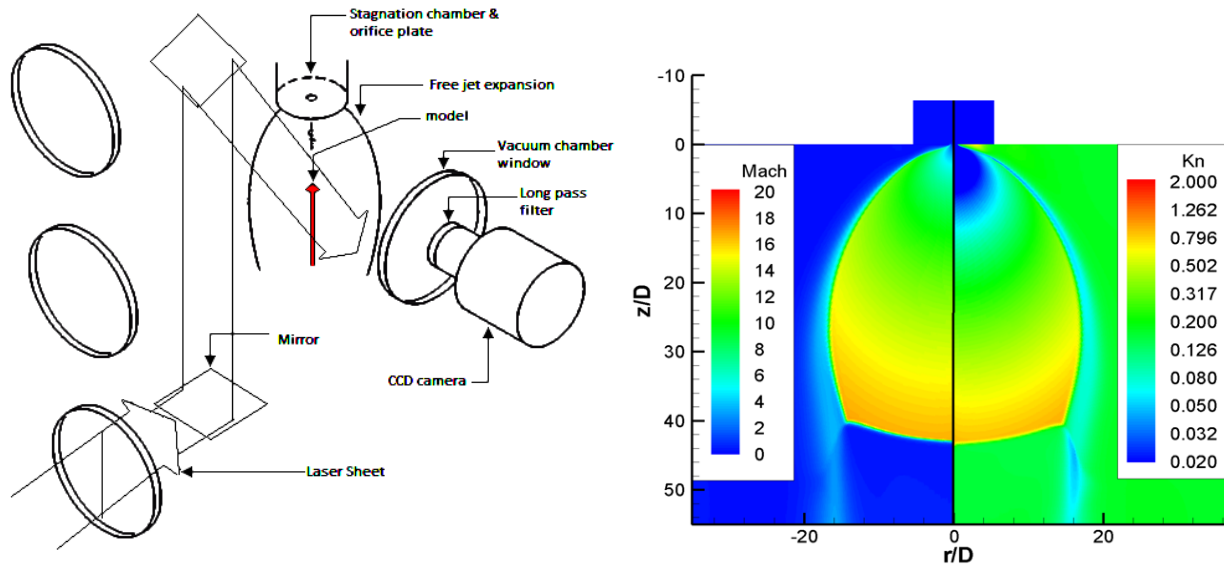

(a) Schematic of the experimental setup[9]

(b) Calculated Mach number and Knudsen number contours in the test section[10]

Figure 2.   Experimental facility.

Experimental results are obtained using the planar laser-induced iodine fluorescence (PLIIF) technique.[8] The PLIIF technique is a non-intrusive, spatially-resolved, time-averaged optical method for obtaining measurements in hypersonic, rarefied flows. The technique has been used for both qualitative and quantitative measurements.[8–11] PLIIF involves seeding iodine into a flowfield and exciting the molecules to a higher energy with an argon ion laser. The laser beam is turned into a thin laser sheet and passed through the flowfield of interest. The resulting fluorescence is imaged at 90° using a cooled scientific-grade charge-coupled device (CCD) camera. Measurements of the absorption spectrum are made as the laser is tuned in frequency. By fitting the measured absorption spectra at every point in the flowfield, the velocity, pressure, density, and temperature can be deduced. The technique provides qualitative flow visualization images when the laser is operated in the broadband mode, in which the laser gain profile is much wider than the iodine absorption linewidth. The results to be presented herein have been taken with this approach.

American Institute of Aeronautics and Astronautics

B.   Numerical Method

The numerical simulations are performed using the CFD code LeMANS, developed at the University of Michigan for simulating hypersonic reacting flows.[12, 13] This general purpose, three-dimensional, parallel code solves the laminar Navier-Stokes equations on unstructured computational grids including thermo-chemical nonequilibrium effects with second-order spatial accuracy. The flow is modeled assuming that the continuum approximation is valid. Furthermore, for this work, it is assumed that the translational and rotational energy modes of all species can be described by two different temperatures T_{tra} and T_{rot},[14] respectively, while the vibrational and electronic temperatures of all species are frozen at 297 K throughout the computational domain. In LeMANS, the mixture transport properties can be computed using several options. In this study, Wilke's semi-empirical mixing rule[15] is used with species viscosities calculated using Blottner's model[16] and species thermal conductivities determined using Eucken's relation.[17]

The finite-volume method applied to unstructured grids is used to solve the set of partial differential equations. LeMANS can simulate two-dimensional and axisymmetric flows using any mixture of quadrilateral and triangular mesh cells, and three-dimensional flows using any mixture of hexahedra, tetrahedra, prisms, and pyramids. A modified Steger-Warming Flux Vector Splitting scheme[18] is used to discretize the inviscid fluxes across cell faces, which is less dissipative and produces better results in boundary layers compared to the original scheme. The viscous terms are computed using cell-centered and nodal values. In this study, time integration is performed using a point-implicit method. LeMANS is parallelized using METIS[19] to partition the computational mesh, and the Message Passing Interface (MPI) to communicate the necessary information between processors.

III.   Numerical Setup

The aeroshell used in this study is a scaled version of the MSL capsule, and is based on experimental test models.[8] The diameter of the aeroshell is equal to 20 mm, which is equivalent to approximately 0.44% of the MSL capsule. The aeroshell is at an angle-of-attack of 20° in order to simulate the conditions of a lifting trajectory in which the lift vector can be utilized to provide some control of the vehicle during atmospheric descent. The computational geometry includes a "sting" attached to the leeward side of the backshell that is used in the experiments to hold the model in the test section and to supply the flow to the RCS jet. A single RCS jet is located about halfway along the windward side of the aeroshell aftbody. Two different RCS thruster orientations are considered in this study. In the first configuration, the RCS jet is directed approximately parallel to the freestream flow, while in the second configuration, the RCS jet is directed almost transverse to the freestream flow. The geometries for the aeroshell with the parallel and transverse RCS jets are shown in Figures 3(a) and 3(b), respectively. The jet for both configurations is supplied through a sonic nozzle with an exit diameter of 0.5 mm. The computational domain consists of one half of the aeroshell geometry due to the symmetry of the flow in order to reduce the computational cost of the simulations. The upstream boundary of the domain is aligned with the bow shock around the aeroshell based on preliminary solutions. The computational grid contains approximately 9 million hexahedral cells, with clustering near the aeroshell surface and in the vicinity of the RCS jet. Each simulation takes approximately 14,000 CPU-hours to reach a steady-state solution.

I_2-seeded N_2 gas is used in the numerical simulations with a seeding ratio of 200 ppm for both the freestream and the RCS jet flows in order to accurately model the experimental conditions. The freejet conditions in the experimental facility are simulated in LeMANS using the relations of Ashkenas and Sherman.[20] A previous study showed that the freestream conditions calculated using these relations widen the bow shock around the aeroshell and slightly decrease the drag coefficient compared to constant freestream conditions.[21] The Mach number at a distance z away from the orifice along the centerline of the freejet is given by Equation 1,

$$M = A\left(\frac{z - z_0}{D}\right)^{\gamma-1} - \frac{1}{2}\left(\frac{\gamma+1}{\gamma-1}\right)\left[A\left(\frac{z - z_0}{D}\right)^{\gamma-1}\right]^{-1} \tag{1}$$

where D is the diameter of the freejet orifice, and A and z_0/D are constants determined for values of the ratio of specific heats γ, and are equal to 3.65 and 0.40, respectively, for $\gamma = 1.4$. All other fluid properties along the freejet axis can be computed using the Mach number defined in Equation 1, the stagnation conditions in the wind tunnel, and the isentropic relations. The density distribution at a fixed distance from the orifice
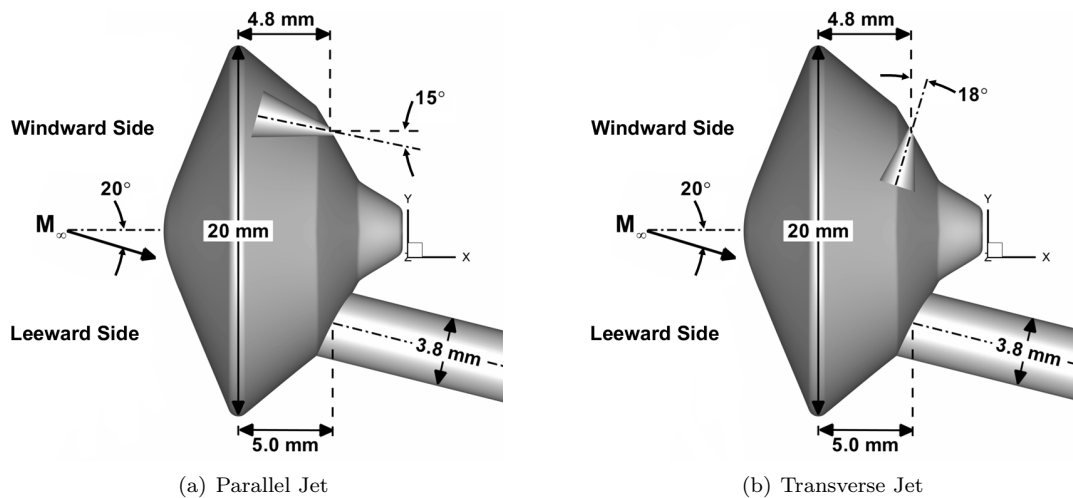
American Institute of Aeronautics and Astronautics

(a) Parallel Jet (b) Transverse Jet

Figure 3. Aeroshell geometry with parallel and transverse RCS jets.

exit is a function of the streamline angle θ with respect to the freejet axis as shown in Equation 2,

$$\frac{\rho\left(\theta\right)}{\rho\left(0\right)} = \cos^2\left(\frac{\pi\theta}{2\Phi}\right) \tag{2}$$

where Φ is also a constant determined for each value of γ, and is equal to 1.662 for $\gamma = 1.4$. For this study, a reference freestream Mach number of 12 at the aeroshell leading edge is used in order to minimize the interaction of the bow shock around the test model and the barrel shock created in the test section in the experiments. The freestream rotational temperature is assumed to be equal to the translational temperature. The aeroshell wall is assumed to be at a constant temperature of 297 K. A set of reference freestream conditions is obtained using isentropic relations for a reference freestream Mach number of 12. These reference conditions are presented in Table 1 and are used to compute non-dimensional quantities, such as the drag coefficient. The low Reynolds number based on these reference conditions and the aeroshell diameter indicates that the freestream flow is laminar.

Table 1. Reference freestream conditions.

Parameter	Value
M_{ref}	12
T_{ref}, K	10
q_{ref}, Pa	127
Re_{ref}	1200

Early work on the Space Shuttle Orbiter had indicated that one of the main scaling parameters for testing of a reaction control system is the ratio of the RCS jet momentum to the freestream momentum (i.e. $(\dot{m}U)_{jet}/(\dot{m}U)_{\infty}$).[22] This scaling parameter was also used to test the performance of the RCS jets for MSL.[7] The final design for the MSL RCS consists of eight total thrusters arranged in four pairs, with each thruster capable of delivering a maximum thrust force of 290 N.[5] The exit diameter for each MSL RCS nozzle is 65 mm. Table 2 presents freestream and RCS jet (nozzle-exit) conditions that MSL is expected to encounter during flight. The mass flow rate in Table 2 is based on the aeroshell frontal area and the nozzle-exit area for the freestream and RCS jet conditions, respectively.

In order to match the ratio of jet momentum to freestream momentum expected to be experienced in

Table 2. Expected freestream and RCS jet at maximum thrust conditions for MSL during flight.[7]

Parameter	Freestream	RCS Jet
γ	1.313	1.346
M	10.0	4.47
P_0, Pa	1.8×10^7	1.1×10^6
$\dot{m}U$, N	2.9×10^5	289

flight, the stagnation pressure of the RCS jet for the current study can be calculated as,

$$P_{0,jet} = \left(\frac{\gamma_e}{\gamma_\infty} \frac{M_e^2}{M_\infty^2} \frac{P_e}{P_\infty} \frac{\sum\limits_{jets} S_e}{S} \right)_{flight} \left(\frac{\gamma_{ref}}{\gamma_e} \frac{M_{ref}^2}{M_e^2} \frac{S}{S_e} \frac{P_{0,jet}}{P_e} P_{ref} \right) \tag{3}$$

where,

$$\frac{P_0}{P} = \left(1 + \frac{\gamma - 1}{2} M^2 \right)^{\frac{\gamma}{\gamma-1}} \tag{4}$$

Using these relations, the stagnation pressure of the RCS jet should be equal to 4,440 Pa for the current study in order to obtain the same momentum ratio as expected in flight. However, this pressure value is smaller than the smallest increment in the pressure gage used in the experimental setup at the University of Virginia, which is below the acceptable range of confidence. Therefore, in order to minimize the uncertainty in the experimental setup to within an acceptable range, the stagnation pressure of the RCS jet for the current study is increased to 8,040 Pa, which corresponds to an 80% increase in the momentum ratio. A higher RCS jet stagnation pressure of 161,000 Pa is also considered in this study, which is well within the confidence range of the experimental setup. The conditions of the RCS jet can be non-dimensionalized using the thrust coefficient, which is defined as the ratio of the thrust force to the product of the reference freestream dynamic pressure (i.e. q_{ref}) and the aeroshell frontal aera. The two RCS jet stagnation pressures considered in this study correspond to thrust coefficient values of 0.05 and 1.0. Table 3 presents the design total pressure ratio, Reynolds number, mass flow rate, and momentum ratio based on the RCS nozzle-exit conditions for the two thrust coefficients investigated in this study. The relatively large Reynolds number for the 1.0 thrust coefficient case may indicate the potential transition of the jet from laminar to turbulent flow.

Table 3. Design conditions for the parallel and transverse RCS jets.

C_T	$P_{0,jet}/P_0$	Re_{jet}	$\dot{m}_{jet}$, mg/s	$(\dot{m}U)_{jet}/(\dot{m}U)_{ref}$
0.05	0.04	570	4.0	0.014
1.0	0.88	11,000	81	0.284

IV. Results

The goal of this study is to better understand the fluid interactions induced by RCS jets on Mars-entry aeroshells. The numerical results are also used in qualitative comparisons with experimental data to assess the accuracy of the computational method. This section presents the flowfield, surface, and aerodynamic properties for the baseline configurations (i.e. without the RCS jet), as well as for the aeroshell with parallel and transverse RCS jets. The section also describes the effects of the fluid interactions produced by the parallel and transverse jets on the control effectiveness of the RCS. The surface properties are presented as non-dimensional pressure and skin friction coefficients, given in Equations 5 and 6, respectively,

$$C_P = \frac{P}{q_{ref}} \tag{5}$$

American Institute of Aeronautics and Astronautics

$$C_f = \frac{\tau}{q_{ref}} \qquad (6)$$

A. Baseline Configuration

This section describes the flowfield, surface, and aerodynamic properties of the aeroshell without the RCS jet (i.e. baseline configuration) at an angle-of-attack of 20°. These results will be used in the following sections to understand how the fluid interactions produced by the RCS jets affect the properties of the aeroshell. Figure 4 presents Mach number contours for the baseline configuration. The figure shows that the flow around the aeroshell is characterized by the bow shock around the capsule and a series of expansion and compression waves that develop around the aeroshell shoulders.
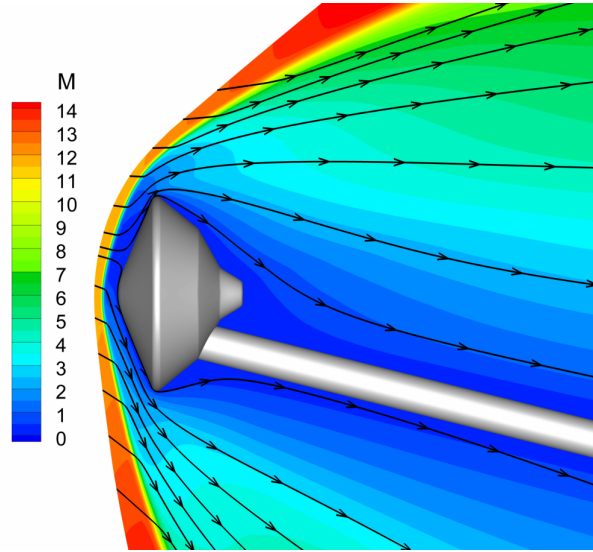
Figure 4. Mach number contours for the no-jet case at 20° angle-of-attack.

Contours of the pressure coefficient along the aeroshell forebody and aftbody for the no-jet case at 20° angle-of-attack are presented in Figure 5. Figure 5(a) shows a large high surface pressure region on the windward side of the aeroshell, with a maximum pressure coefficient value of approximately 2.0 at the stagnation point. The pressure distribution along the aeroshell aftbody shown in Figure 5(b) is characterized by very low pressure coefficient values relative to the forebody. In fact, the integrated aftbody pressure downstream of the aeroshell shoulder is over two orders of magnitude smaller than the integrated forebody pressure. This result suggests that the effects of the sting on the aerodynamic properties of the aeroshell are negligible since the force on the aftbody is very small compared to the forebody.

The aerodynamic properties of the aeroshell without the RCS jet at an angle-of-attack of 20° are provided in Table 4. The moment coefficient of the aeroshell is determined by,

$$C_M = \frac{M_z}{q_{ref} D_{model} S} \qquad (7)$$

where D_{model} is the diameter of the aeroshell (i.e. 20 mm), and M_z is the moment (about the Z-axis) given by,

$$M_z = (X - X_{CG}) F_N - (Y - Y_{CG}) F_A \qquad (8)$$

where F_N and F_A are the normal (Y-direction) and axial (X-direction) components of the aerodynamic force, respectively, and $(X, Y)_{CG}$ is the location of the center of gravity of the aeroshell *without* the sting. This choice for the location of the center of gravity is appropriate since the presence of the sting has a negligible effect on the total aerodynamic forces acting on the aeroshell, which are shown schematically in Figure 6. The results given in Table 4 show that the normal force acting on the aeroshell is negative due to the large surface pressures on the windward side of the aeroshell forebody. The lift force on the aeroshell, however, is positive due to the contribution from the relatively large axial force. The results also show that
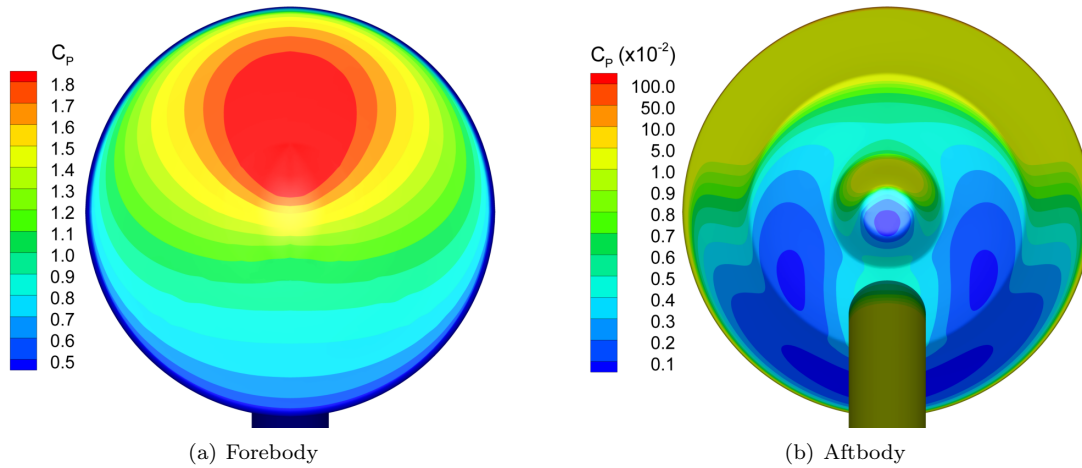
American Institute of Aeronautics and Astronautics

(a) Forebody   (b) Aftbody

Figure 5. Forebody and aftbody pressure coefficient contours for the no-jet case at 20° angle-of-attack.

the moment of the aeroshell is negative (i.e. clockwise-direction), which is also caused by the large surface pressures on the windward portion of the aeroshell forebody.

Table 4. Aerodynamic properties of the no-jet case at 20° angle-of-attack.

C_A	C_N	C_D	C_L	L/D	C_M
1.28	-0.17	1.26	0.28	0.22	-0.060
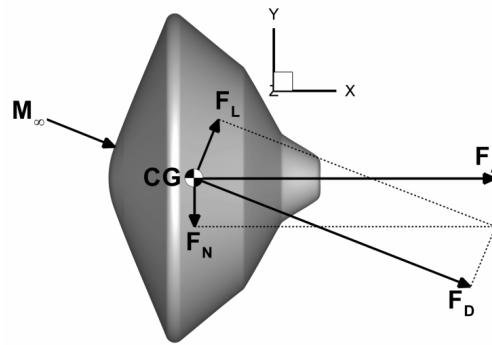
Figure 6. Schematic of the aerodynamic forces acting on the aeroshell at 20° angle-of-attack ($X_{CG}/D_{model} = 0.26$, $Y_{CG}/D_{model} = 0.0$).

B. Parallel RCS Jet

Mach number contours and velocity streamlines around the aeroshell with the parallel RCS jet are presented in Figure 7 for thrust coefficients of 0.05 and 1.0. The RCS jet at both thrust coefficients expands from sonic conditions at the nozzle-exit to supersonic and hypersonic conditions downstream of the aeroshell in the wake. The velocity streamlines indicate that the parallel RCS jet obstructs the path of the flow from the freestream around the aeroshell aftbody, particularly at $C_T = 1.0$, and causes it to move outward along the jet boundary. As a result, the Mach number decreases and the flow is compressed in the region along the aeroshell aftbody upstream of the RCS jet boundary. Figure 7(a) shows that the parallel jet at $C_T = 0.05$ only disturbs the portion of the flow close to the aeroshell on the windward side, and does not have a

American Institute of Aeronautics and Astronautics

significant effect on the overall structure of the flowfield. At $C_T = 1.0$, the parallel RCS jet expands to higher Mach numbers and changes the flow in the entire windward portion of the wake region, as can be seen in Figure 7(b). The parallel jet, however, does not affect the profile of the bow shock around the aeroshell.
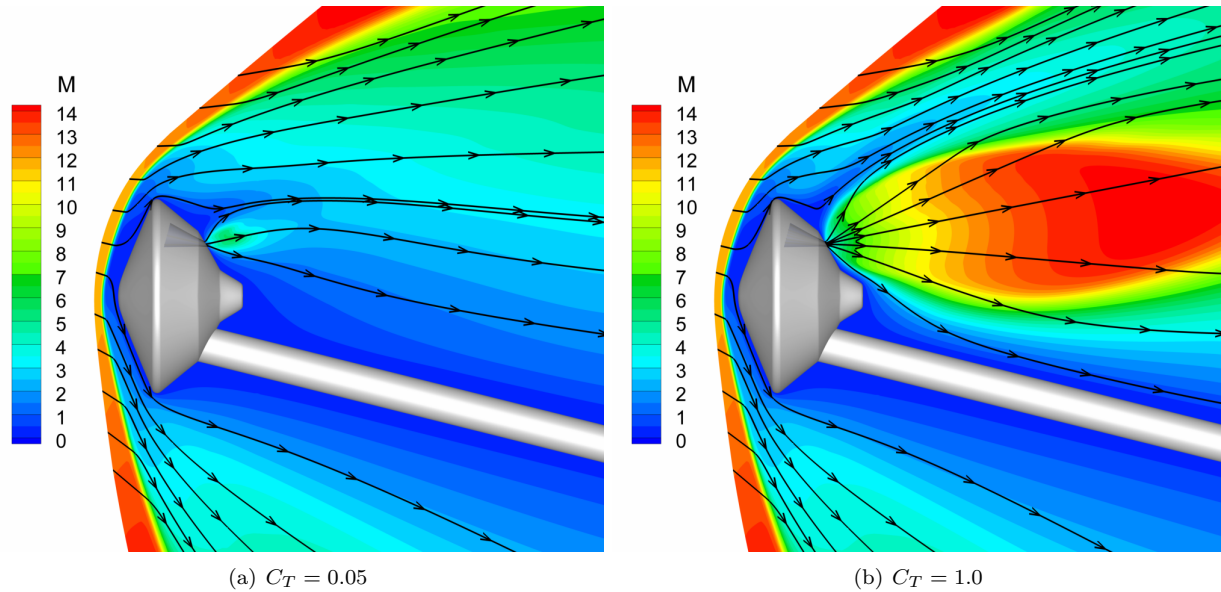

(a) $C_T = 0.05$ (b) $C_T = 1.0$

Figure 7. Mach number contours for the parallel RCS jet at $C_T = 0.05$ and 1.0.

The distribution of the RCS jet species mole fraction can be calculated by tagging the N_2 molecules originating from the RCS (i.e. same properties as molecular nitrogen but different name), and is shown in Figure 8 for the parallel jet at $C_T = 0.05$ and 1.0. The contours for the lower thrust condition presented in Figure 8(a) show that the mole fraction of the RCS jet is relatively high close to the aeroshell, and decreases downstream in the wake as the jet expands. At the higher thrust coefficient, the RCS jet mole fraction is large (greater than 0.95) in roughly the entire windward wake region of the computational domain. Figure 8(b) also shows that a significant amount of the jet species impinge on the surface of the aftbody downstream of the RCS nozzle. This impingement is important for the design of the aftbody thermal protection system since the hot exhaust from the RCS nozzle that may be experienced in flight can significantly increase the heat flux to the aeroshell surface.

Figure 9 presents pressure coefficient contours along the aeroshell forebody and aftbody for the parallel RCS jet at the 0.05 and 1.0 thrust coefficients. Figure 9(a) shows that the forebody pressure distribution is unaffected by the RCS jet, and is, in fact, identical to the forebody distribution for the no-jet case shown in Figure 5(a). Along the aftbody, however, the RCS jet alters the pressure distribution, particularly at the higher thrust conditions. At $C_T = 0.05$, the RCS jet only affects the region directly around the nozzle-exit, where the impingement of the jet species causes an increase in the surface pressure. At $C_T = 1.0$, the RCS jet increases the pressure on most of the windward side of the aftbody compared to the baseline configuration, particularly downstream of the nozzle-exit near the parachute cone. As a result of the parallel RCS jet, the integrated pressure along the aeroshell aftbody increases by 31% and 520% for $C_T = 0.05$ and 1.0, respectively, compared to the no-jet case.

Figure 10 presents the distributions of the pressure and skin friction coefficients along the centerline of the aeroshell aftbody (excluding the RCS nozzle) for the parallel RCS jet at $C_T = 0.05$ and 1.0. The figure also presents the corresponding distributions for the baseline (i.e. no-jet) configuration for comparison. The pressure coefficient for the parallel RCS jet at $C_T = 0.05$, shown in Figure 10(a), sharply decreases from high values near the nozzle-exit to relatively small values comparable to the baseline configuration. At the high thrust coefficient, the pressure also decreases from high values near the RCS nozzle-exit, but then increases upstream of the nozzle to as much as twice as large as the corresponding value for the no-jet case. This increase in pressure upstream of the nozzle-exit is caused by a combination of added mass from the RCS jet and the obstruction of the flow from the freestream by the parallel jet. Downstream of the nozzle-exit, the impingement of the jet species on the surface increases the surface pressure by approximately one order of
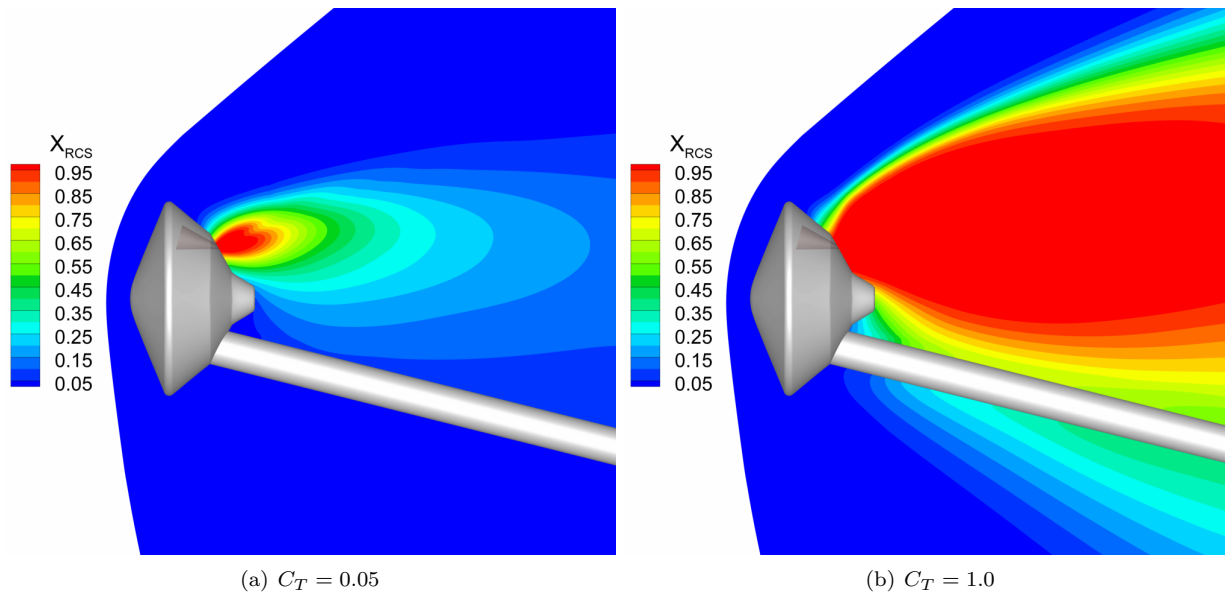
(a) $C_T = 0.05$

(b) $C_T = 1.0$

Figure 8. RCS jet species mole fraction contours for the parallel RCS jet at $C_T = 0.05$ and 1.0.
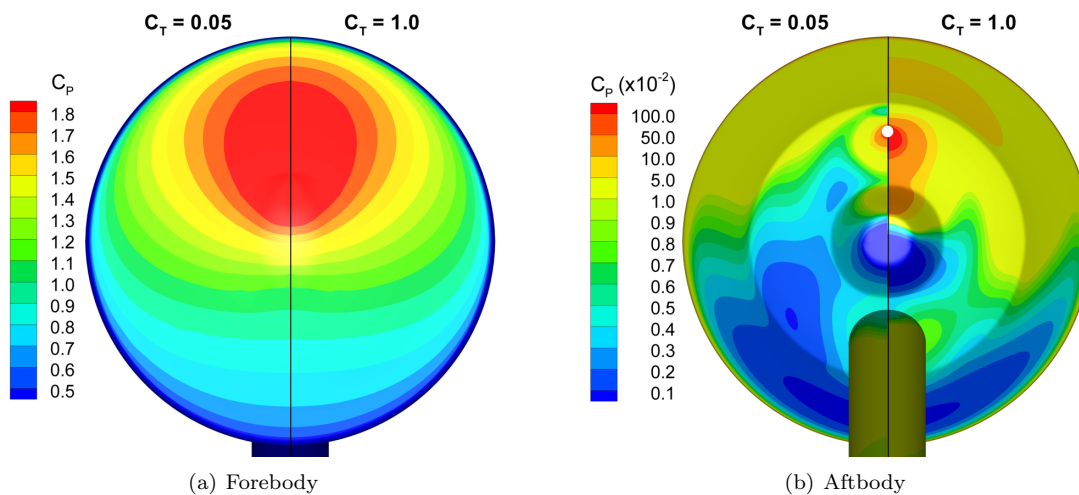

(a) Forebody

(b) Aftbody

Figure 9. Forebody and aftbody pressure coefficient contours for the parallel RCS jet at $C_T = 0.05$ and 1.0.

magnitude compared to the baseline configuration.

The magnitude of the coefficient of skin friction for the parallel RCS jet at the two thrust conditions also decreases from high values near the nozzle-exit, as shown in Figure 10(b). The shear stress directly upstream of the nozzle-exit is negative at both thrust coefficients since the jet first moves upstream towards the aeroshell shoulder as it expands from the RCS nozzle. At the low thrust coefficient, the distribution of the shear stress away from the nozzle-exit is similar to the distribution for the no-jet case. At $C_T = 1.0$, however, the obstruction of the flow from the freestream by the parallel jet decreases the shear stress upstream of the RCS nozzle by approximately a factor of 2 compared to the no-jet case. Downstream of the nozzle-exit, the expansion of the parallel jet at $C_T = 1.0$ along the aftbody increases the shear stress by roughly one order of magnitude compared to the baseline configuration.
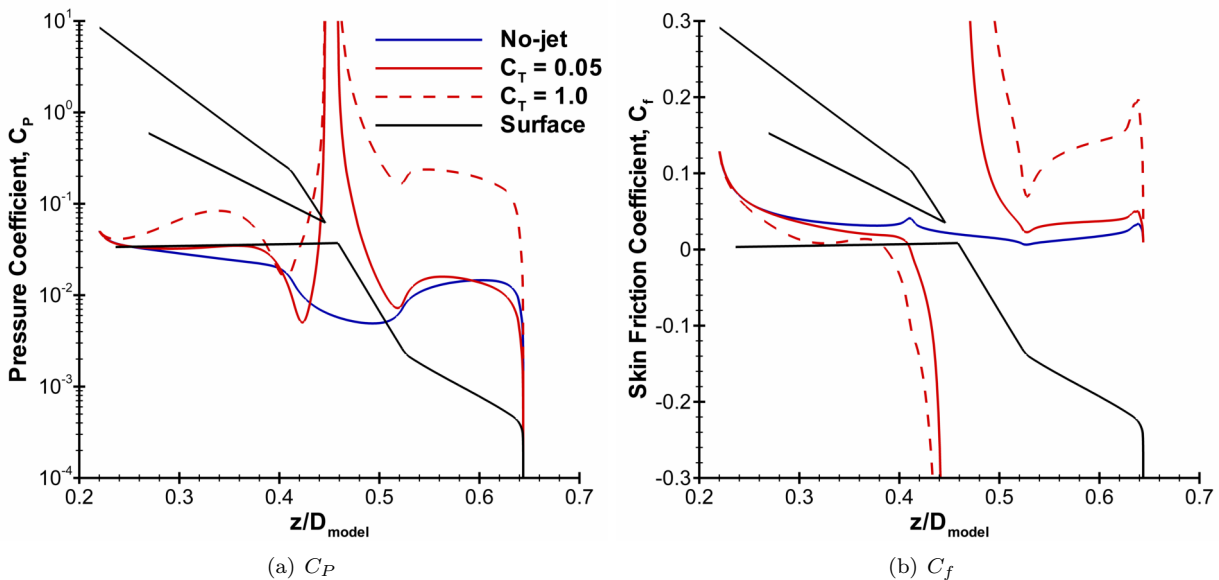

(a) C_P

(b) C_f

Figure 10. The distributions of pressure and skin friction coefficients along the centerline of the aeroshell aftbody for the parallel RCS jet at $C_T = 0.05$ and 1.0.

The changes in the surface properties along the aftbody caused by the parallel RCS jet may have an important effect on the aerodynamic properties of the aeroshell. Table 5 presents a summary of the aerodynamic properties of the aeroshell with the parallel RCS jet at $C_T = 0.05$ and $C_T = 1.0$, as well as the properties for the no-jet case for comparison. Note that the axial and normal force coefficients presented in Table 5 do not include the thrust coefficient of the RCS thruster. The results indicate that the parallel RCS jet at $C_T = 0.05$ has almost no effect on the aerodynamic properties of the aeroshell. At the higher thrust coefficient, however, the increased surface pressure on the windward side of the aeroshell aftbody decreases the aerodynamic axial force by approximately 4% and increases the modulus of the aerodynamic normal force by about 24%. As a result, the aerodynamic drag and lift forces acting on the aeroshell decrease by approximately 2% and 21%, respectively. The interactions produced by the RCS jet at the higher thrust coefficient also decrease the modulus of the moment by 5%.

Table 5. Aerodynamic properties of the aeroshell with the parallel RCS jet.

C_T	C_A	C_N	C_D	C_L	L/D	C_M
No-jet	1.28	-0.17	1.26	0.28	0.22	-0.060
0.05	1.28	-0.17	1.26	0.28	0.22	-0.060
1.0	1.23	-0.21	1.23	0.22	0.18	-0.057

American Institute of Aeronautics and Astronautics

C.   Transverse RCS Jet

The Mach number distributions around the aeroshell with the transverse RCS jet for thrust coefficients of 0.05 and 1.0 are presented in Figure 11. The RCS jet at both thrust conditions exhausts almost normal to the flow around the aeroshell, and expands from sonic conditions at the nozzle-exit to hypersonic conditions downstream of the aeroshell. Similar to the parallel jet, the velocity streamlines shown in Figure 11 indicate that the transverse RCS jet obstructs the path of the flow from the freestream around the aeroshell aftbody, which decreases the Mach number and compresses the flow upstream of the jet boundary near the aftbody surface. This obstruction, however, is stronger for the transverse configuration since the jet can penetrate farther upstream than the parallel jet. Figure 11(b) also shows that the RCS jet impinges on the bow shock, which pushes the portion of the shock downstream of the RCS nozzle-exit away from the aeroshell.
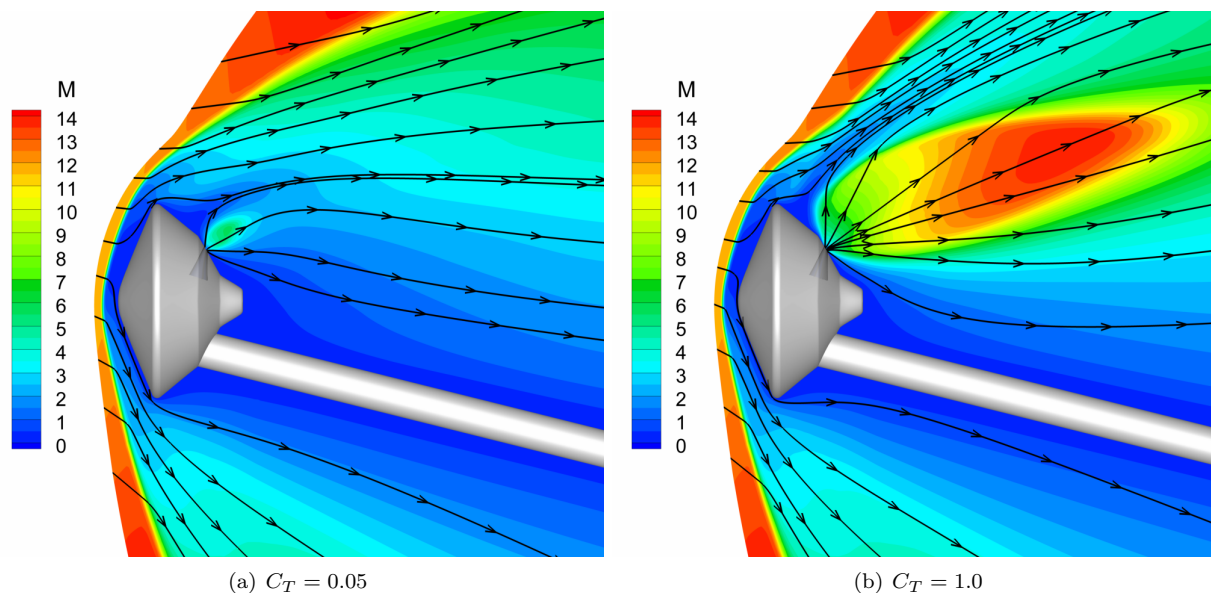

(a) $C_T = 0.05$ (b) $C_T = 1.0$

Figure 11.   Mach number contours for the transverse RCS jet at $C_T = 0.05$ and 1.0.

Figure 12 shows the jet species mole fraction for the transverse RCS jet at the two thrust conditions investigated in this study. Similar to the parallel jet, the mole fraction for the transverse RCS jet at the lower thrust coefficient is large relatively close to the nozzle-exit and decreases as the jet expands downstream of the aeroshell. At the higher thrust coefficient, the value of the jet species mole fraction remains large for approximately the entire windward portion of the wake that is included in the computational domain. Figure 12 also indicates that a larger amount of jet species is transported upstream of the nozzle-exit towards the aeroshell shoulder for the transverse RCS jet than previously observed for the parallel jet. For instance, the distance upstream of the nozzle-exit where the jet species mole fraction is equal to 0.5 is greater for the transverse jet by approximately 50% for $C_T = 0.05$ and 65% for $C_T = 1.0$ compared to the parallel jet. The figure, however, also shows that the amount of jet species downstream of the nozzle-exit near the parachute cone is relatively smaller for the transverse jet than observed for the parallel jet.

Figure 13 presents the distributions of pressure coefficient along the aeroshell forebody and aftbody for the transverse RCS jet at thrust coefficients of 0.05 and 1.0. Figure 13(a) shows that the transverse RCS jet does not affect the pressure distribution along the aeroshell forebody since the contours are identical to the ones shown in Figure 5(a) for the no-jet case. The transverse RCS jet, however, does affect the surface pressure along the aeroshell aftbody. Figure 13(b) indicates that the transverse RCS jet increases the pressure along the aftbody, particularly upstream of the nozzle-exit near the aeroshell shoulder compared to the baseline configuration. The figure also shows that the transverse jet at the higher thrust coefficient causes overall larger surface pressure values than the jet at the lower thrust conditions. As a result, the integrated pressure along the aeroshell aftbody increases by 43% and 560% for the transverse RCS jet at $C_T = 0.05$ and 1.0, respectively, compared to the no-jet case.

The coefficients of pressure and skin friction along the aftbody centerline for the transverse RCS jet at
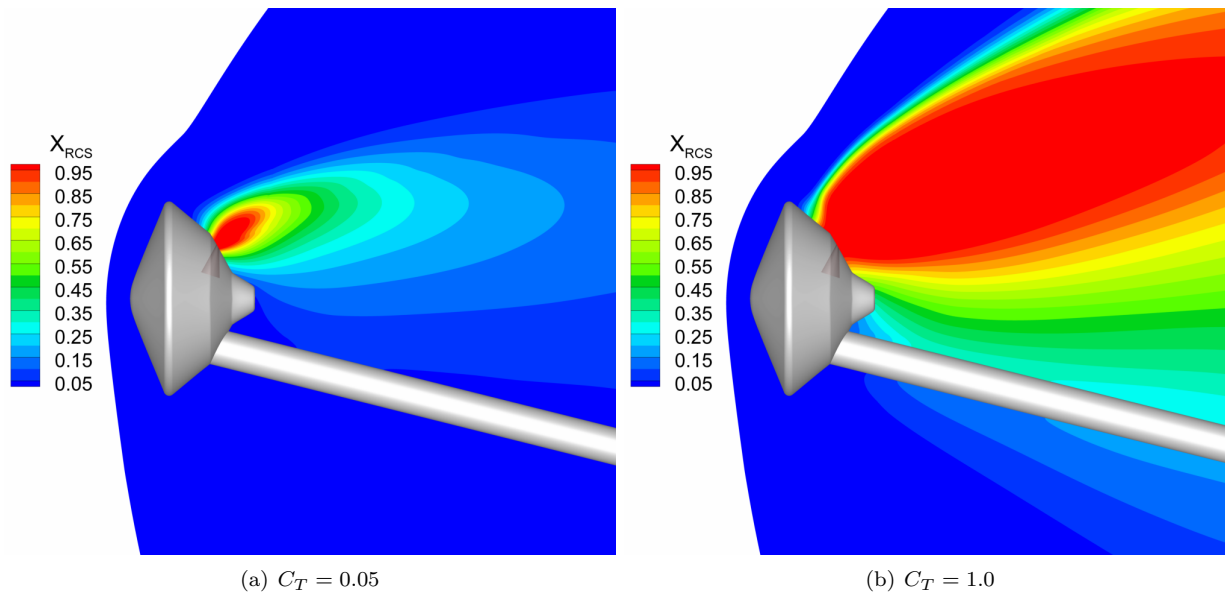
American Institute of Aeronautics and Astronautics

(a) $C_T = 0.05$

(b) $C_T = 1.0$

Figure 12. RCS jet species mole fraction contours for the transverse RCS jet at $C_T = 0.05$ and 1.0.
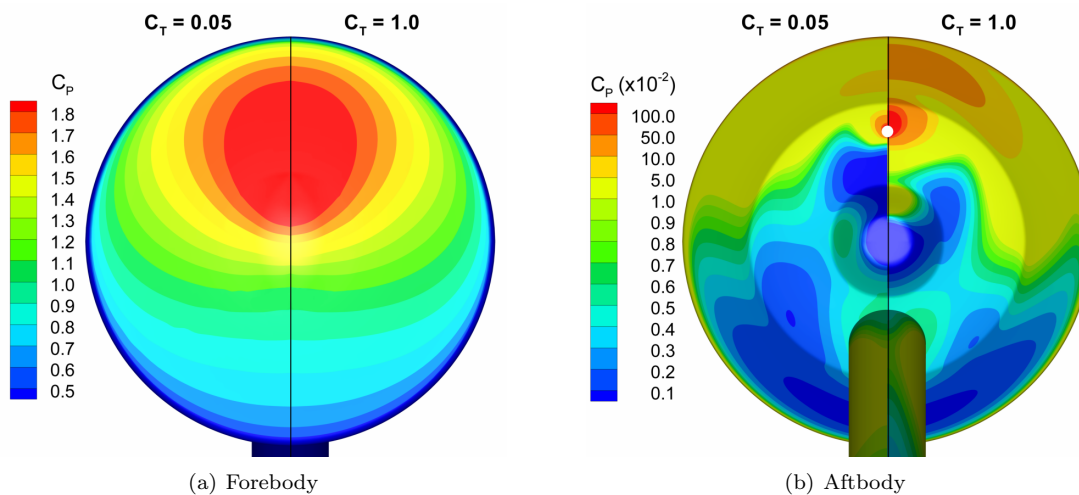

(a) Forebody

(b) Aftbody

Figure 13. Forebody and aftbody pressure coefficient contours for the transverse RCS jet at $C_T = 0.05$ and 1.0.

$C_T = 0.05$ and 1.0 are presented in Figure 14. Upstream of the nozzle-exit, the pressure coefficient for the transverse jet at both thrust conditions, shown in Figure 14(b), first decreases and then increases due to a combination of added mass from the RCS and the compression of the flow near the surface caused by the obstruction of the flow from the freestream by the transverse jet. Downstream of the nozzle-exit, the transverse jet at $C_T = 0.05$ decreases the pressure by approximately one order of magnitude compared to the no-jet case since only a relatively small amount of the jet species impinge on the surface. However, the pressure downstream of the nozzle-exit for the transverse RCS jet increases at $C_T = 1.0$ to values comparable to the baseline configuration since more jet species are transported downstream.

Figure 14(b) shows that the coefficient of skin friction for the transverse RCS jet at both thrust conditions decreases in magnitude away from the nozzle-exit. The negative sign of the shear stress indicates that the transverse jet first flows upstream of the nozzle-exit before encountering the flow from the freestream. Upstream of the nozzle-exit, the shear stress for the transverse jet at both thrust conditions decreases from large values caused by the expansion of the transverse jet from the RCS nozzle to low values produced by the slow speeds of the flow from the freestream. Downstream of the nozzle-exit, the shear stress distributions for the transverse RCS jet at $C_T = 0.05$ and 1.0 are similar to the distribution for the baseline configuration. However, the overall skin friction coefficients for the transverse jet at $C_T = 1.0$ are approximately twice as large as the values for both $C_T = 0.05$ and the no-jet cases.

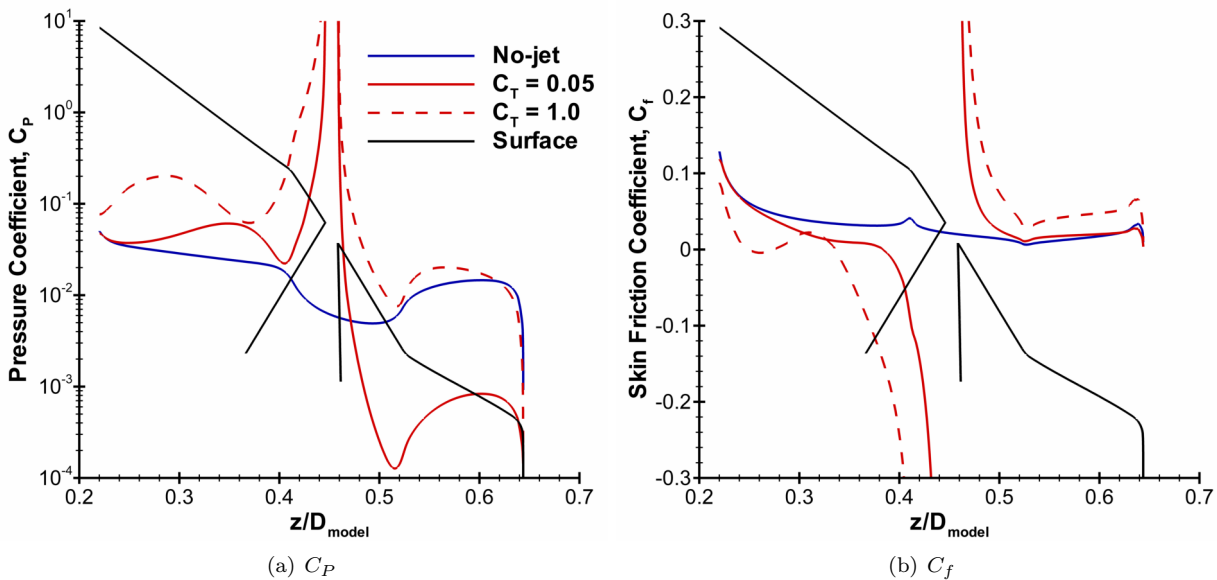(a) C_P (b) C_f

Figure 14. The distributions of pressure and skin friction coefficients along the centerline of the aeroshell aftbody for the transverse RCS jet at $C_T = 0.05$ and 1.0.

The fluid interactions produced by the transverse RCS jet may also affect the aerodynamic properties of the aeroshell. Table 6 presents the coefficients of the aerodynamic forces and moment acting on the aeroshell with the transverse RCS jet at $C_T = 0.05$ and 1.0, as well as the coefficients for the baseline configuration for comparison. Similar to the parallel jet, the aerodynamic axial and normal forces do not include any contribution from the RCS thrust. The results show that for the lower thrust conditions, the larger aftbody pressures caused by the transverse RCS jet decrease the aerodynamic axial and drag forces acting on the aeroshell by less than 1%. The transverse jet at $C_T = 0.05$ also decreases the modulus of the moment by approximately 3%. At the higher thrust conditions, the transverse RCS jet decreases the axial force by approximately 5% and increases the modulus of the normal force by about 18% compared to the no-jet case. As a result, the drag and lift forces acting on the aeroshell decrease by 4% and 18%, respectively. The transverse RCS jet also decreases the modulus of the moment by about 22% at $C_T = 1.0$ compared to the baseline configuration.

American Institute of Aeronautics and Astronautics

Table 6. Aerodynamic properties of the aeroshell with the transverse RCS jet.

C_T	C_A	C_N	C_D	C_L	L/D	C_M
No-jet	1.28	-0.17	1.26	0.28	0.22	-0.060
0.05	1.27	-0.17	1.25	0.28	0.22	-0.058
1.0	1.22	-0.20	1.21	0.23	0.19	-0.047

D.   Performance of the Parallel and Transverse RCS Jets

The main function of the reaction control system is to provide vehicle control and steering by producing moments about the center of gravity of the capsule. Specifically, the parallel RCS jet generates a positive moment (i.e. counter-clockwise direction) about the center of gravity, whereas the transverse RCS jet produces a negative moment (i.e. clockwise direction), as can be seen in Figure 15. However, the aerodynamic interference induced by the RCS jet plume can have a significant impact on the performance of the RCS jet. Therefore, the effectiveness of the reaction control system can be examined by defining a "control gain" as,

$$\text{Gain} = \frac{C_{M_{thrust}} + C_{M_{interference}}}{C_{M_{thrust}}} \tag{9}$$

where, $C_{M_{thrust}}$ is the coefficient of the moment generated by the thrust force of the RCS jet, and $C_{M_{interference}}$ is the coefficient of the moment produced by the aerodynamic interference caused by the RCS jet given by,

$$C_{M_{interference}} = C_M - C_{M_{no\text{-}jet}} \tag{10}$$

Ideally, the RCS jet does not generate any aerodynamic interference and the control gain is equal to unity. However, if the control gain is less than unity, then the aerodynamic interference creates a deficit of control authority. Similarly, if the control gain is greater than unity, then the aerodynamic interference causes a surplus of authority. A similar approach was also used to examine the effectiveness of the reaction control system for the MSL mission.[2]
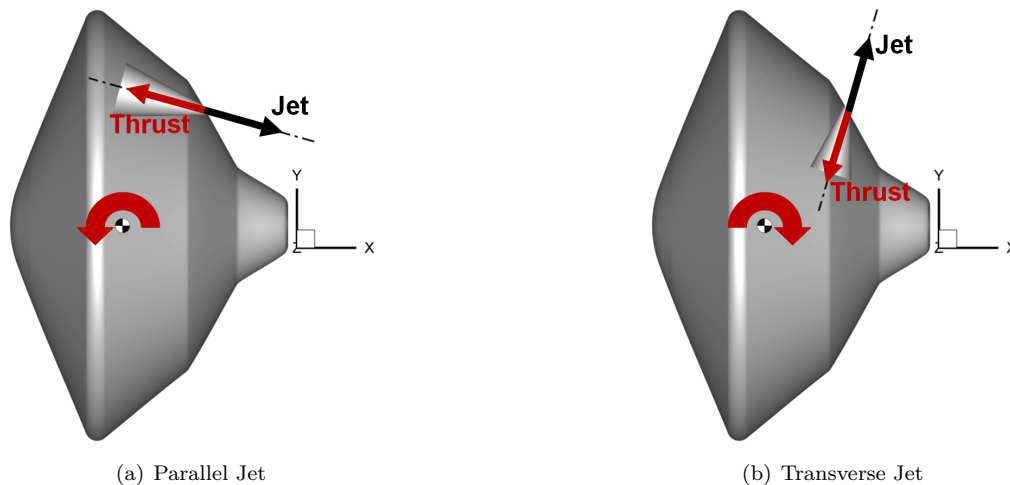

(a) Parallel Jet

(b) Transverse Jet

Figure 15. Direction of the moment produced by the thrust force from the parallel and transverse RCS jets about the center of gravity of the aeroshell.

The control effectiveness of the transverse and parallel RCS jets is summarized in Figure 16. Figure 16(a) presents the ratio of the moment produced by the aerodynamic interference (defined in Equation 10) to the moment induced by the thrust force from the RCS for the parallel and transverse jets. The figure shows that the ratio is small for the parallel RCS jet and does not exceed 0.01 for both $C_T = 0.05$ and

American Institute of Aeronautics and Astronautics

1.0. The ratio is also positive for the parallel jet, which implies that the two moments act along the same direction (counter-clockwise). As a result, the control gain for the parallel RCS jet, shown in Figure 16(b), is approximately equal to unity, which is ideal because the effectiveness of the reaction control system is similar to the design condition. For the transverse RCS jet, however, the ratio of interference moment to thrust moment is relatively large and equal to almost -0.40 for $C_T = 0.05$ and -0.14 for $C_T = 1.0$. Figure 16(a) also shows that the interference moment (counter-clockwise) and the thrust moment (clockwise) act in opposite directions since the ratio of the two moments is negative. As a result, the aerodynamic interference induced by the transverse RCS jet creates a control deficit, as can be seen in Figure 16(b), which is not ideal because a fraction of the thrust is used to counteract the aerodynamic interference, and the effectiveness of the reaction control system diminishes.


(a) $C_{M_{interference}}/C_{M_{thrust}}$
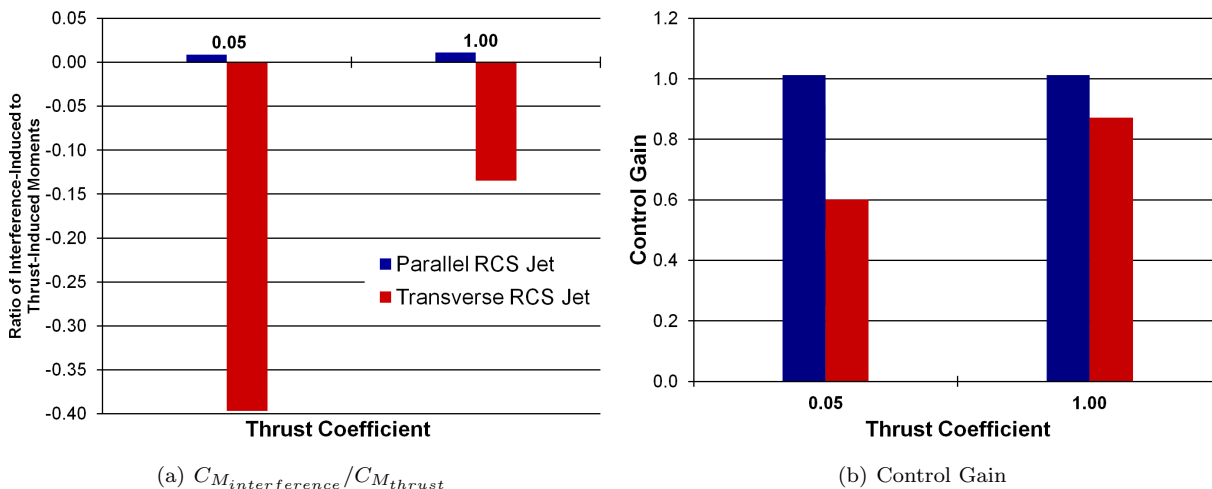
(b) Control Gain

Figure 16. The ratio of interference moment to thrust-induced moment and the control gain for the parallel and transverse RCS jets at $C_T = 0.05$ and 1.0.

The trends observed in the performance of the reaction control system with parallel and transverse RCS jets are caused by two factors. First, the moment produced by the thrust force from the parallel RCS jet is approximately three times larger than the moment produced by the thrust from the transverse jet at both thrust conditions. This difference in the thrust-induced moment is caused by the contribution of the axial and normal components of the thrust force and the length of the moment arm. For the parallel RCS jet, both the axial and normal components of the thrust force contribute to a positive thrust-induced moment with respect to the center of gravity of the aeroshell. However, for the transverse RCS jet, the normal component of the thrust force produces a negative moment, while the axial component generates a positive moment about the center of gravity. The modulus of the moment produced by the axial component of the thrust force from the transverse jet is approximately equal to 45% of the modulus of the moment generated by the thrust component along the normal direction at both $C_T = 0.05$ and 1.0. This means that the two components of the thrust force from the transverse RCS jet provide counteracting moments that result in a smaller net thrust-induced moment. The parallel RCS jet also has a larger moment arm than the transverse jet. Figure 17 presents the lengths of the moment arm along the axial (i.e. X-axis) and normal (i.e. Y-axis) directions with respect to the center of gravity along the aeroshell surface. The midpoint of the RCS nozzle-exit is located approximately 0.2 and 0.3 aeroshell diameters away from the center of gravity of the aeroshell along the axial and normal directions, respectively, for both RCS configurations. Even though both RCS jets produce the same amount of thrust (at each given thrust coefficient), the parallel RCS jet has a larger moment arm than the transverse jet because most of the thrust force is directed along the axial direction. These results suggest that the control effectiveness of the reaction control system can be made close to ideal by selecting an orientation of the RCS jet such that the contribution to the thrust-induced moment by all of the components of the thrust force are along the same direction, and by maximizing the moment arm of each thruster.

The second cause of the trends observed in the performance of the RCS thrusters is that the transverse jet produces a larger interference moment compared to the parallel jet. In order to understand the source

(a) X-moment arm
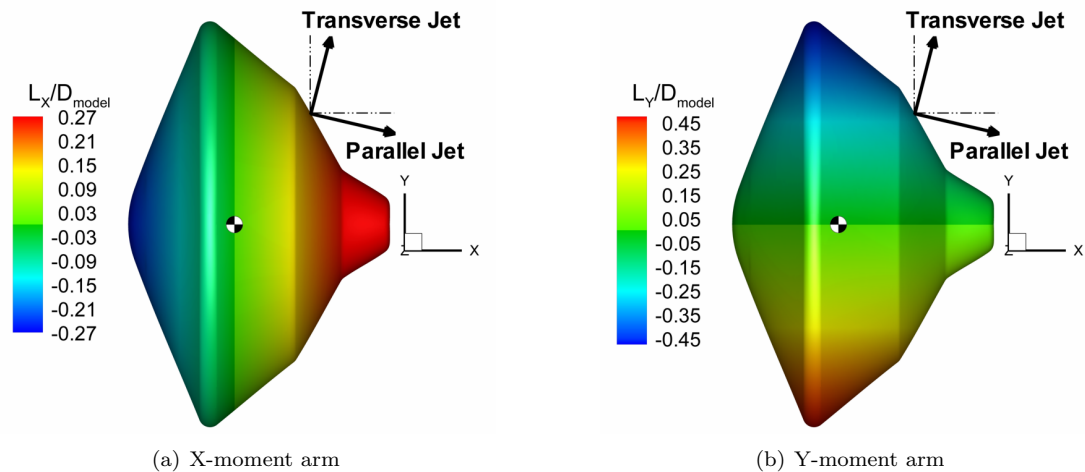
(b) Y-moment arm

Figure 17. Lengths of the moment arm with respect to the center of gravity of the aeroshell along the X and Y directions.

of this interference, Figure 18 presents the distribution of the moment per unit area along the centerline of the aeroshell aftbody for the parallel and transverse RCS jets at the two thrust conditions investigated in this study. The figure also presents the corresponding distribution for the no-jet case for reference. The figure shows that the moment along the aftbody centerline is negative and relatively small for the baseline configuration. At the low thrust coefficient for the parallel RCS jet, the pressure and shear stress distributions produced by the jet generate a relatively large positive moment directly upstream of the nozzle-exit which is counteracted by a similarly large negative moment directly downstream of the nozzle. As a result, the integrated moment along the centerline for the parallel RCS jet is only 40% larger than the integrated moment for the no-jet case. For the transverse jet at $C_T = 0.05$, however, the augmented surface pressures upstream of the nozzle-exit create a relatively larger positive moment than the negative moment downstream of the nozzle-exit. Consequently, the integrated moment along the centerline for the transverse RCS jet is approximately three times larger than the value for the baseline configuration. At the higher thrust coefficient, shown in Figure 18(b), the surface pressure and shear stress distributions caused by the parallel and transverse RCS jets produce a positive moment upstream of the nozzle-exit and a negative moment downstream of the nozzle-exit along the aftbody centerline. However, the figure shows that the transverse RCS jet induces a large positive moment over a longer distance upstream of the nozzle-exit compared to the parallel jet, which causes the integrated moment along the centerline for the transverse jet to be over twice as large as the value for the parallel jet. This result indicates that the parallel RCS jet produces relatively smaller net interference moments compared to the transverse jet because it can induce opposing moments with respect to the center of gravity of the aeroshell that can counteract one another. Therefore, the control effectiveness of the reaction control system can be also improved by either minimizing the fluid interactions induced by the jet, or by designing the layout of the RCS such that the fluid interactions produce counteracting effects that result in a small net interference.

E. Comparisons with Experimental Data

The numerical results presented in the previous sections are compared to experimental data in order to assess the physical accuracy of the computational method. Qualitative comparisons between the CFD (LeMANS) results and experimental data of the bow shock profile around the aeroshell without the RCS jet (i.e. baseline configuration) is shown in Figure 19. The image is a PLIIF visualization obtained at the University of Virginia by Reed et al.[8] The flow is from left to right and the freestream flow is seeded with iodine so that the flowfield features are visible. The sting used in the experiments to mount the capsule in the test section has been removed from the image and the aeroshell model has been superimposed for illustrative purposes. The fluorescence shown in the image is directly proportional to the iodine number density for regions of the flow where the Mach number is between 6 and 17,[23, 24] which means that each brightness level in the PLIIF image

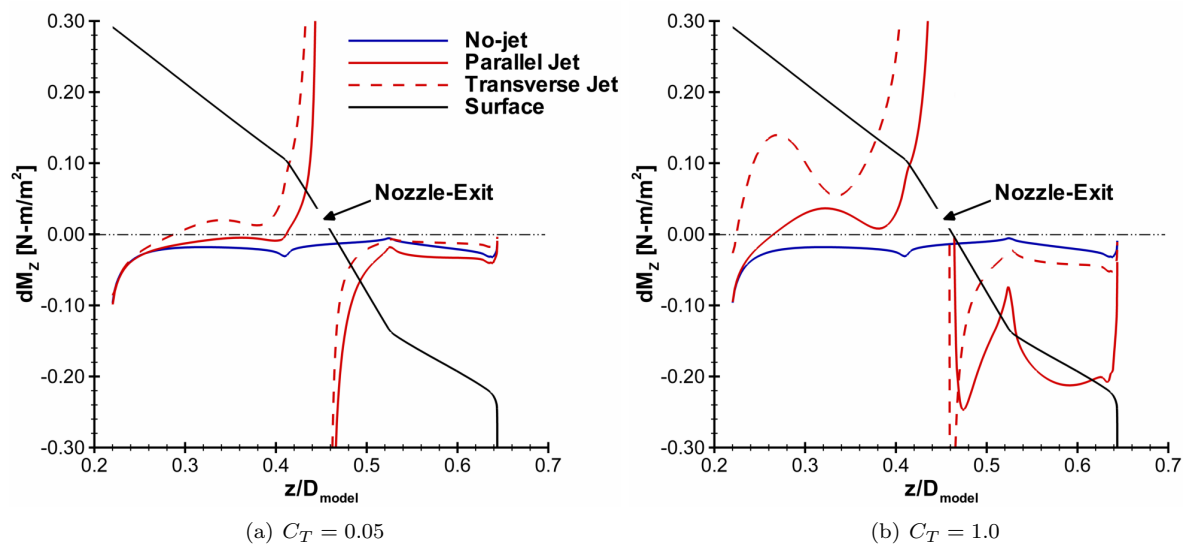American Institute of Aeronautics and Astronautics

Figure 18. Comparison of the distribution of the moment per unit area along the centerline of the aeroshell aftbody between the parallel and transverse RCS jets at $C_T = 0.05$ and 1.0.

corresponds to a specific iodine density value in the hypersonic regions of the flow. The bow shock profile can be determined from this image as the region upstream and around the aeroshell where the brightness changes. Figure 19 also presents velocity streamlines (Figure 19(a)) and a contour of iodine density (Figure 19(b)) obtained from the numerical results and overlaid on the PLIIF visualization. The contour level for the CFD results corresponds to the iodine density value at the point along the aeroshell centerline where the iodine density in the freestream begins to increase. This contour is representative of the bow shock along the aeroshell since the fluorescence in the PLIIF image is directly proportional to the iodine density in this region of the flow. The bow shock profile for the numerical results can be also determined from the velocity streamlines as the location in the freestream where the slope of each streamline changes. Both the velocity streamlines and the iodine density contour indicate excellent agreement with the bow shock profile observed in the PLIIF visualization in the portion of the shock upstream of the aeroshell. However, the agreement between the two sets of results decreases downstream of the aeroshell shoulder. The figure shows that the bow shock predicted by LeMANS is farther away from the aeroshell than observed experimentally.

The planar laser-induced iodine fluorescence technique is also used to obtain visualizations of flow around a Mars-entry aeroshell with parallel and transverse RCS jets.[8] Figure 20 presents velocity streamlines and the iodine density contour representative of the bow shock profile obtained from the numerical results and overlaid on a PLIIF visualization for the parallel RCS jet at $C_T = 1.0$. The PLIIF image indicates a small interaction between the parallel RCS jet and the bow shock because the jet does not impinge on the shock. The figure shows good qualitative agreement in the bow shock profile between the numerical and experimental results, with some differences downstream of the aeroshell similar to those observed in the comparisons for the baseline configuration.

Similar qualitative bow shock profile comparisons between the numerical results and experimental visualizations for the transverse RCS jet at $C_T = 1.0$ are presented in Figure 21. The figure shows velocity streamlines and the iodine density contour indicative of the bow shock profile calculated by LeMANS and superimposed over a PLIIF visualization. The PLIIF image indicates that the plume of the transverse RCS jet impinges on the bow shock and changes its profile. This jet-shock interaction is greater than observed for the parallel RCS jet. Good agreement in the bow shock profile between the numerical results and the PLIIF image can be observed upstream of the aeroshell shoulder. Downstream of the capsule, however, LeMANS predicts a larger penetration depth of the transverse RCS jet, which increases the distance of the bow shock from the aeroshell, compared to the PLIIF visualization. As a result, the distance of the bow shock from the aeroshell is greater for the CFD results than observed experimentally.

The disagreement in the bow shock profile downstream of the aeroshell between the numerical and experimental results may be caused by several factors. The first possible source of the disagreement between the
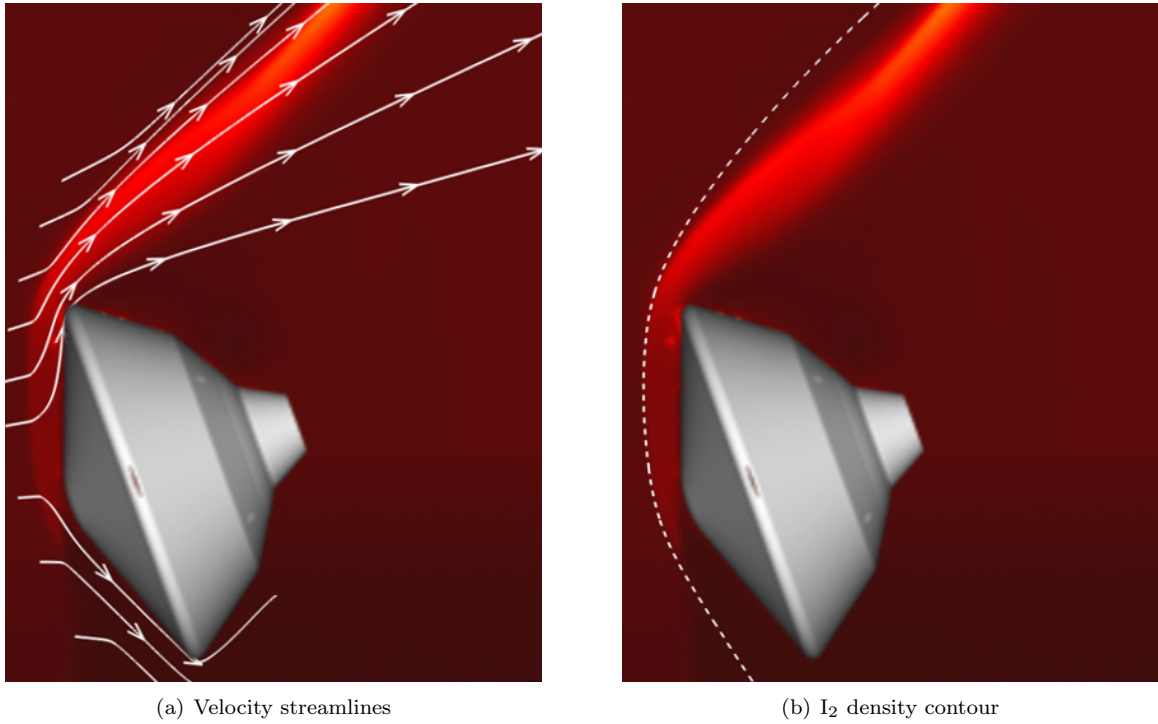
(a) Velocity streamlines

(b) I$_2$ density contour

Figure 19. Comparison of the bow shock profile for the no-jet case at 20° angle-of-attack between the numerical (velocity streamlines and I$_2$ density contour) and experimental (PLIIF image) results.
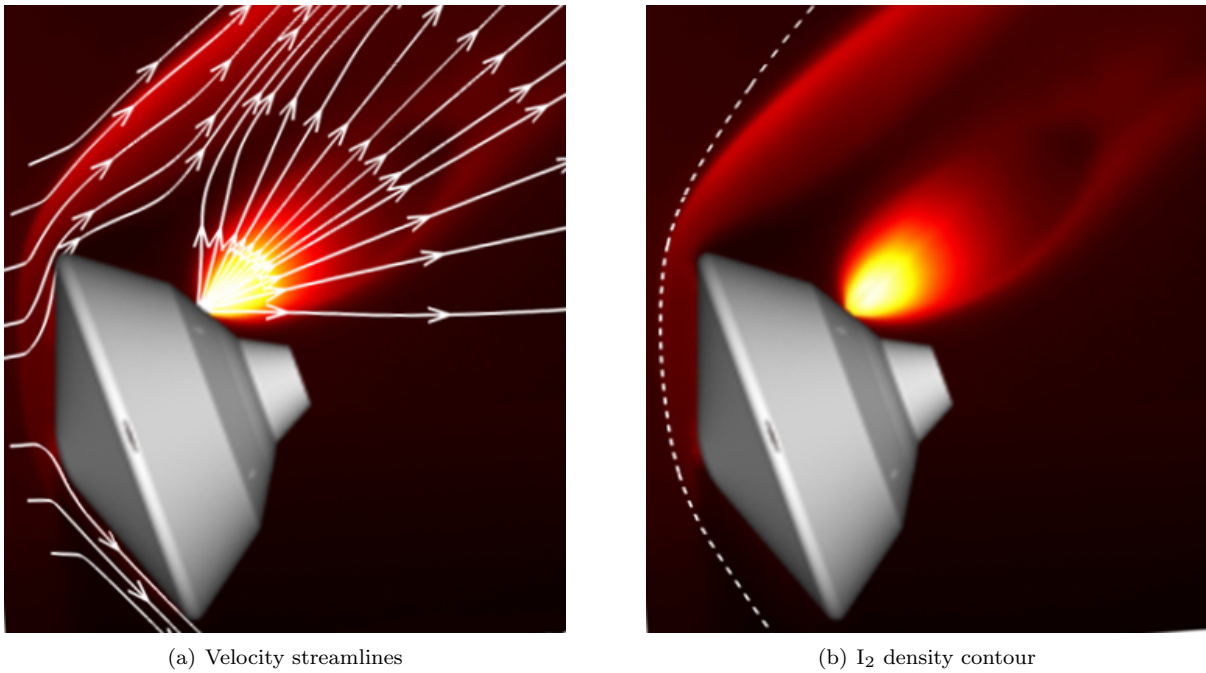

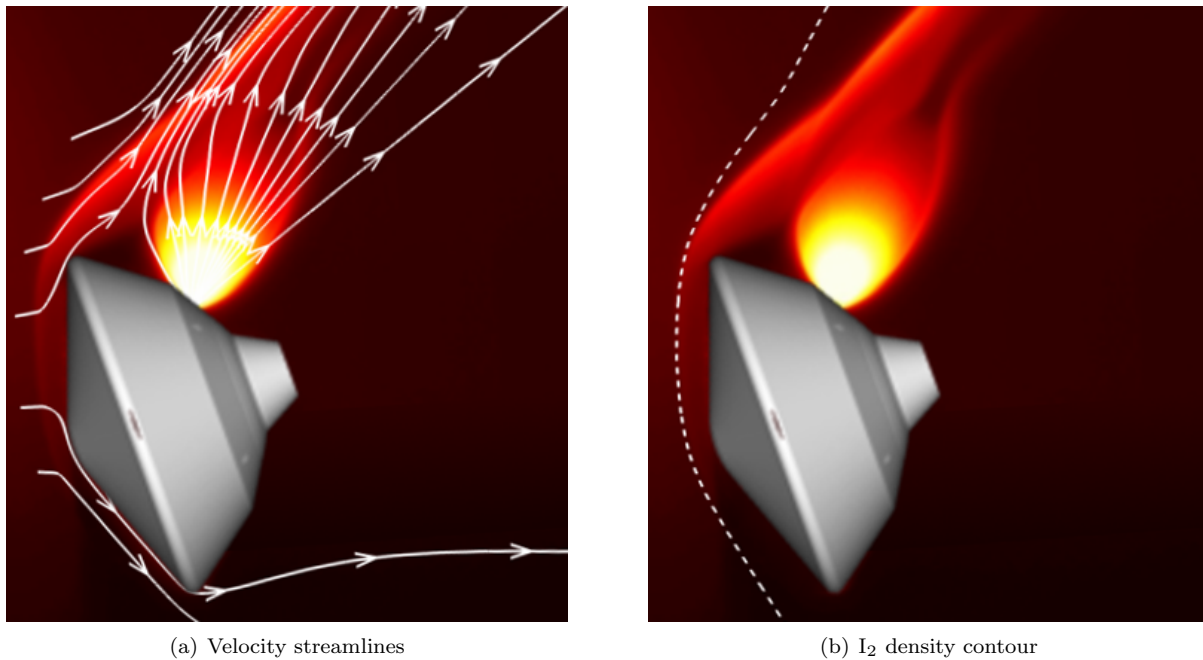(a) Velocity streamlines

(b) I$_2$ density contour

Figure 20. Comparison of the bow shock profile for the parallel RCS jet at $C_T = 1.0$ between the numerical (velocity streamlines and I$_2$ density contour) and experimental (PLIIF image) results.

(a) Velocity streamlines

(b) I$_2$ density contour

Figure 21. Comparison of bow shock profile for the transverse RCS jet at $C_T = 1.0$ between the numerical (velocity streamlines and I$_2$ density contour) and experimental (PLIIF image) results.

CFD result and the PLIIF visualization is the Ashkenas and Sherman relations that provide the freestream conditions in the numerical simulations, which may not be appropriate for relatively large streamline angles greater than approximately 10°.[25] Another possible cause of the disagreement between the numerical and experimental results is the interaction of the bow shock with the barrel shock in the experiments, which is shown in Figure 22. This interaction between the two shock structures in the experimental facility, referred to as the triple-point, can change the profile of the bow shock around the aeroshell.

V.   Conclusion

The fluid interactions induced by the reaction control system of a Mars-entry aeroshell in hypersonic flow of I$_2$-seeded N$_2$ gas was investigated. The aeroshell diameter used in the study is 20 mm and the angle-of-attack was set to 20° to simulate the conditions of a lifting trajectory. A single, sonic RCS jet was placed approximately half-way along the aeroshell aftbody. Two different RCS jet orientations were considered in this study to understand how the RCS configuration affects the flowfield, surface, and aerodynamic properties of the aeroshell. For the first configuration, the jet was directed almost parallel to the main freestream flow, while the second configuration used a jet that was almost normal to the flow. Two different thrust coefficients were also considered for each RCS configuration. The lower thrust coefficient, equal to 0.05, was chosen to provide a ratio of RCS jet momentum to freestream momentum close to the value expected to be experienced in flight by MSL. A thrust coefficient of 1.0 was also chosen to compare the numerical results with experimental data.

The results showed that both the parallel and transverse RCS jets altered the flow on the windward side of the wake, particularly at $C_T = 1.0$. The jets expanded from sonic conditions at the nozzle-exit to higher Mach numbers downstream of the aeroshell, and obstructed the path of the flow from the freestream along the aftbody. This obstruction was larger for the transverse RCS jet since it could penetrate farther upstream compared to the parallel jet. The results also showed that both the parallel and transverse RCS jets did not have any effect on the pressure distribution along the aeroshell forebody. However, the RCS jets altered the surface properties and increased the overall pressure along the windward side of the aeroshell aftbody. The aerodynamic properties of the aeroshell with both the parallel and transverse RCS jets at $C_T = 0.05$ were overall similar to the properties for the baseline configuration, but the transverse jet decreased the moment
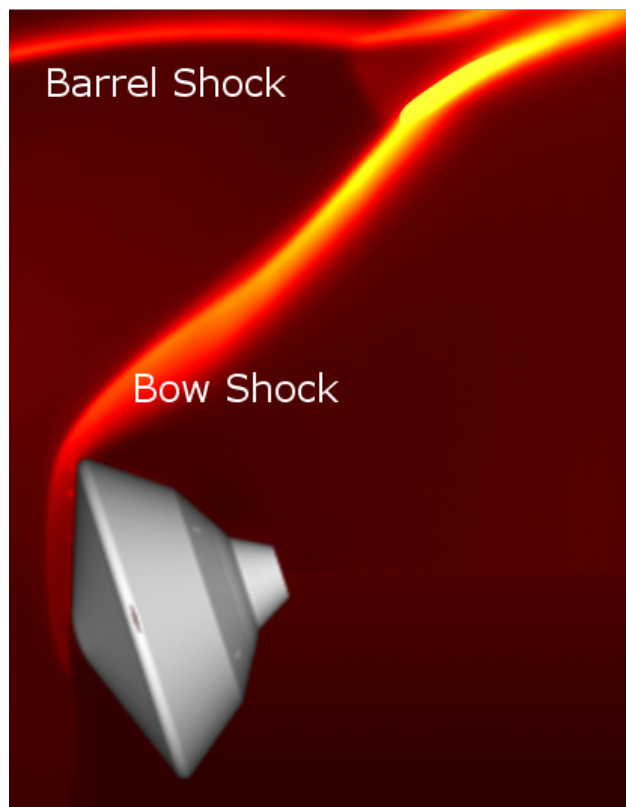
American Institute of Aeronautics and Astronautics

Figure 22. PLIIF image of the interaction between the bow shock and the barrel shock in the experimental facility.

American Institute of Aeronautics and Astronautics

on the aeroshell by 3%. At the 1.0 thrust coefficient, however, the parallel and transverse RCS jets decreased the aerodynamic moment acting on the aeroshell by 5% and 22%, respetively. The results also showed that the combination of large thrust-induced moment and small interference moment caused the performance of the parallel RCS jet to be close to an ideal performance at both $C_T = 0.05$ and $C_T = 1.0$. The transverse RCS jet, however, suffered from a control deficit at both thrust conditions due to a combination of small thrust-induced moment and large interference moment. These results suggest that the control effectiveness of a reaction control system can be increased by selecting the orientation of the RCS jet with large moment arms such that the contribution to the thrust-induced moment by all of the components of the thrust force are along the same direction. The RCS control effectiveness can be also increased by either minimizing the fluid interactions induced by the jet, or by designing the layout of the RCS such that the fluid interactions produce counteracting effects that result in a small net interference. Finally, qualitative bow shock profile comparisons between the numerical results and experimental visualizations obtained using PLIIF were performed to assess the physical accuracy of the computational method. The comparisons indicated overall good agreement between the numerical and experimental results. The comparisons, however, showed some disagreement between the two methods in the portion of the bow shock away from the aeroshell centerline. These differences are believed to be caused by the inaccuracy of the Ashkenas and Sherman relations in LeMANS for large streamline angles, and the influence of the triple-point on the bow shock profile in the experimental facility.

VI.   Future Work

For future work, more qualitative, as well as quantitative comparisons between numerical and experimental results of flowfield and aerodynamic properties of Mars-entry aeroshells with RCS jets will be performed in order to continue the assessment of the computational method. Flight conditions and enthalpy levels will also be considered in order to study the aerothermodynamic effects of RCS jets.

VII.   Acknowledgments

References

[1] Prakash, R., Burkhart, P., Chen, A., Comeaux, K., Guernsey, C., Kipp, D., Lorenzoni, L., Mendeck, G., Powell, R., Rivellini, T., San Martin, A., Sell, S., Steltzner, A., and Way, D., "Mars Science Laboratory Entry, Descent, and Landing System Overview," *IEEEAC Paper 1531*, March 2008.

[2] Dyakonov, A. A., Schoenenberger, M., Scallion, W. I., Van Norman, J. W., Novak, L. A., and Tang, C. Y., "Aerodynamic Interference Due to MSL Reaction Control System," *AIAA Paper 2009-3915*, June 2009.

[3] Braun, R. D. and Manning, R. M., "Mars Exploration Entry, Descent, and Landing Challenges," *Journal of spacecraft and rockets*, Vol. 44, No. 2, March-April 2007, pp. 310–323.

[4] Edquist, K. T., Dyakonov, A. A., Wright, M. J., and Tang, C. Y., "Aerothermodynamic Environments Definition for the Mars Science Laboratory Entry Capsule," *AIAA Paper 2007-1206*, January 2007.

[5] Edquist, K. T., Dyakonov, A. A., Wright, M. J., and Tang, C. Y., "Aerothermodynamic Design of the Mars Science Laboratory Backshell and Parachute Cone," *AIAA Paper 2009-4078*, June 2009.

[6] Johansen, C. T., Danehy, P. M., Ashcraft, S. W., Bathel, B. F., Inman, J. A., and Jones, S. B., "PLIF Study of Mars Science Laboratory Capsule Reaction Control System Jets," *AIAA Paper 2011-3890*, June 2011.

[7] Schoenenberger, M., Dyakonov, A., Buning, P., Scallion, W., and Van Norman, J., "Aerodynamic Challenges for the Mars Science Laboratory Entry, Descent and Landing," *AIAA Paper 2009-3914*, June 2009.

[8] Reed, E. M., Codoni, J., McDaniel, J. C., Alkandry, H., and Boyd, I. D., "Investigation of the Interactions of Reaction Control Systems with Mars Science Laboratory Aeroshell," *AIAA Paper 2010-1558*, January 2010.

[9] Codoni, J. R., Reed, E. M., McDaniel, J. C., Alkandry, H., and Boyd, I. D., "Investigations of Peripheral 4-jet Sonic and Supersonic Propulsive Deceleration Jets on a Mars Science Laboratory Aeroshell," *AIAA 2011-1036*, January 2011.

[10] McDaniel, J. C., Glass, C. E., Staack, D., and Miller, C. G., "Experimental and Computational Comparisons of an Underexpanded Jet Flowfield," *AIAA Paper 2002-0305*, January 2002.

[11] Cecil, D. E. and McDaniel, J. C., "Planar Laser-Induced Iodine Fluorescence Measurements in Rarefied Hypersonic Flow," *Rarefied Gas Dynamics: 24th International Symposium*, Toronto, Canada, 2005, pp. 1325–1350.

[12] Scalabrin, L. C. and Boyd, I. D., "Development of an Unstructured Navier-Stokes Solver for Hypersonic Nonequilibrium Aerothermodynamics," *AIAA Paper 2005-5203*, June 2005.

American Institute of Aeronautics and Astronautics

[13]Scalabrin, L. C. and Boyd, I. D., "Numerical Simulation of Weakly Ionized Hypersonic Flow for Reentry Configurations," *AIAA Paper 2006-3773*, June 2006.

[14]Holman, T. D. and Boyd, I. D., "Effects of Continuum Breakdown on the Surface Properties of a Hypersonic Sphere," *Journal of Thermophysics and Heat Transfer*, Vol. 23, No. 4, October-December 2009, pp. 660–673.

[15]Wilke, C. R., "A Viscosity Equation for Gas Mixtures," *Journal of Chemical Physics*, Vol. 18 No. 4, 1950, pp. 517–519.

[16]Blottner, F. G., Johnson, M., and Ellis, M., "Chemically Reacting Viscous Flow Program for Multi-Component Gas Mixtures," Tech. rep., SC-RR-70-754, Sandia Laboratories, Albuquerque, New Mexico, 1971.

[17]Vincenti, W. G. and Kruger, C. H., *Introduction to Physical Gas Dynamics*, Krieger Publishing Company, 2002.

[18]MacCormack, R. W. and Candler, G. V., "The Solution of the Navier-Stokes Equations using Gauss-Seidel Line Relaxation," *Computers and Fluids*, Vol. 17, 1989, pp. 135–150.

[19]Karypis, G. and Kumar, V., "METIS: A Software Package for Partitioning Unstructured Graphs, Partitioning Meshes, and Computing Fill-Reducing Orderings of Sparse Matrices," *University of Minnesota*, 1998.

[20]Ashkenas, H. and Sherman, F. S., "The Structure and Utilization of Supersonic Free Jets in Low Density Wind Tunnels," *Proceedings of the 4th International Symposium on Rarefied Gas Dynamics*, Academic Press, 1966, pp. 84–105.

[21]Alkandry, H., Boyd, I. D., Reed, E. M., and McDaniel, J. C., "Numerical Study of Hypersonic Wind Tunnel Experiments for Mars Entry Aeroshells," *AIAA Paper 2009-3918*, June 2009.

[22]Rausch, J. R., "Space Shuttle Rear Mounted Reaction Control System Jet Interaction Study," CASD-NSC-77-003, General Dynamics, 1977.

[23]McDaniel, J. C., Codoni, J. R., Reed, E. M., Alkandry, H., and Boyd, I. D., "Propulsion Deceleration Studies using Planar Laser-Induced Iodine Fluorescence and Computation Fluid Dynamics," *AIAA 2011-2549*, May 2011.

[24]Hartfield, R. J., Hollo, S. D., and McDaniel, J. C., "Planar Temperature Measurement in Compressible Flows using Laser-Induced Iodine Fluorescence," *Optics Letter*, Vol. 16, January 1991, pp. 106–108.

[25]Legge, H., "Force and Heat Transfer Measurements in Hypersonic Free-Jet Flow," *AIAA Paper 94-2633*, June 1994.

American Institute of Aeronautics and Astronautics